OPEN ACCESS



Magnetar Central Engines in Gamma-Ray Bursts Follow the Universal Relation of Accreting Magnetic Stars

Simone Dall'Osso¹, Giulia Stratta^{1,2,3,4}, Rosalba Perna^{5,6}, Giovanni De Cesare⁴, and Luigi Stella⁷ has instituto Nazionale di Fisica Nucleare—Roma 1, Piazzale Aldo Moro 2, I-00185 Roma, Italy; simoneda@romal.infn.it institut für Theoretische Physik, Goethe Universität, Max-von-Laue-Str. 1, D-60438 Frankfurt am Main, Germany is Istituto di Astrofisica e Planetologia Spaziali, via Fosso del Cavaliere 100, I-00133 Roma, Italy is Inafe—Osservatorio Astornomico di Bologna, viale P.Gobetti, Bologna, Italy Departement of Physics & Astronomy, Stony Brook University, Stony Brook, NY 11794, USA Center for Computational Astrophysics, Flatiron Institute, New York, NY 10010, USA INAF—Osservatorio Astornomico di Roma, via Frascati 33, I-00078, Monte Porzio Catone, Roma, Italy Received 2023 February 14; revised 2023 April 4; accepted 2023 April 11; published 2023 June 5

Abstract

Gamma-ray bursts (GRBs), both long and short, are explosive events whose inner engine is generally expected to be a black hole or a highly magnetic neutron star (magnetar) accreting high-density matter. Recognizing the nature of GRB central engines, and in particular the formation of neutron stars (NSs), is of high astrophysical significance. A possible signature of NSs in GRBs is the presence of a plateau in the early X-ray afterglow. Here we carefully select a subset of long and short GRBs with a clear plateau, and look for an additional NS signature in their prompt emission, namely a transition between the accretion and propeller phases in analogy with accreting, magnetic compact objects in other astrophysical sources. We estimate from the prompt emission the minimum accretion luminosity below which the propeller mechanism sets in, and the NS magnetic field and spin period from the plateau. We demonstrate that these three quantities obey the same universal relation in GRBs as in other accreting compact objects switching from accretion to propeller. This relation provides also an estimate of the radiative efficiency of GRBs, which we find to be several times lower than radiatively efficient accretion in X-ray binaries and in agreement with theoretical expectations. These results provide additional support to the idea that at least some GRBs are powered by magnetars surrounded by an accretion disk.

Unified Astronomy Thesaurus concepts: Gamma-ray bursts (629); Magnetars (992); Stellar accretion disks (1579); High energy astrophysics (739)

1. Introduction

After several decades of observations, modeling and theoretical investigations, gamma-ray bursts (GRBs), the most energetic explosions in the universe, still leave open questions. The two generally distinctive classes of long and short GRBs have been securely associated with the collapse of massive stars for the former (Hjorth et al. 2003; Stanek et al. 2003), and with the merger of two neutron stars (NSs) for the latter (Abbott et al. 2017). However, the fate of the remnant compact object left behind after the stellar collapse or the binary NS merger still remains to be deciphered, a problem with implications also for the equation of state (EOS) of ultradense matter (Lattimer & Prakash 2001) and the generation of gravitational wave signals (e.g., Dall'Osso et al. 2015, 2018).

If the remnant compact object is an NS, it is likely to be highly magnetized. In the case of formation in the collapse of a massive star, this is because of the fast rotation likely necessary to drive a long GRB (MacFadyen & Woosley 1999; Heger et al. 2003), which facilitates magnetic field amplification due to dynamo action (Thompson & Duncan 1995; Raynaud et al. 2020; Aloy & Obergaulinger 2021; Obergaulinger & Aloy 2021; Guilet et al. 2022). In the case of NS–NS mergers, magnetic field amplification via a dynamo has been demonstrated in general relativistic

Original content from this work may be used under the terms of the Creative Commons Attribution 4.0 licence. Any further distribution of this work must maintain attribution to the author(s) and the title of the work, journal citation and DOI.

magnetohydrodynamic simulations of the merger (Giacomazzo & Perna 2013; Zrake & MacFadyen 2013; Giacomazzo et al. 2015; Palenzuela et al. 2015, 2022; Kawamura et al. 2016; Ciolfi et al. 2017; Radice 2017; Aguilera-Miret et al. 2020, 2022).

The possibility that the inner engine driving the GRB emission may be a fast-spinning and highly magnetized NS rather than a black hole has received considerable attention in recent years (Thompson et al. 2004; Bucciantini et al. 2007, 2012; Metzger et al. 2007, 2018; Dall'Osso et al. 2011; Rowlinson et al. 2013; Beniamini et al. 2017; see however, e.g., Kumar et al. 2008; Siegel et al. 2014; Beniamini & Mochkovitch 2017; Beniamini et al. 2020; Oganesyan et al. 2020). If GRBs are indeed powered by a magnetar, there are observational signatures that may point to their presence (e.g., Dai & Lu 1998; Zhang & Mészáros 2001). In particular, since the early-time spin-down luminosity of an NS has a plateau, this behavior may be reflected in the initial plateau of the X-ray afterglow, assuming that its luminosity tracks the energy injection from the NS. By fitting the observed light curves, in particular the plateau luminosity and duration, these models provide estimates of the magnetic fields and spin periods of the putative magnetars (e.g., Dall'Osso et al. 2011; Rowlinson et al. 2013; Gompertz et al. 2014; Lü & Zhang 2014; Gibson et al. 2017). The resulting P- and B-values in the population are found to be correlated in a way that matches the wellestablished "spin-up line" of radio pulsars and magnetic accreting NSs in galactic X-ray binaries (e.g., Bhattacharya & van den Heuvel 1991; Pan et al. 2013), once rescaled for the much larger mass accretion rates of GRBs (Stratta et al. 2018).

In this work we reexamine the impact of a magnetar central engine by considering both prompt and afterglow emissions jointly. Similarly to previous studies (e.g., Bernardini et al. 2013: Stratta et al. 2018), we assume the prompt is powered by accretion energy while the afterglow plateau by the injection of the NS spin energy into the external shock. During the prompt phase, the newly born magnetar strongly interacts with the accretion disk left behind by the progenitor, and may undergo transitions to a propeller regime (Illarionov & Sunyaev 1975; Stella et al. 1986), where disk material cannot enter the magnetosphere and the accretion power is reduced. We thus set to study whether this scenario is compatible with the general luminosity evolution observed in prompt GRB light curves, which can also explain the B-P correlation found by Stratta et al. (2018). Previous suggestions to interpret GRB precursors in a similar framework gave encouraging results in a few GRBs (Bernardini et al. 2013, 2014).

As shown by Stella et al. (1986) and Campana et al. (1998a), for transient X-ray binaries hosting different populations of NSs, the onset of propeller is characterized by a distinctive knee in the decaying phase of the light curve, from which the transition luminosity can be determined. By independently measuring the spin (via their pulsed emission) and magnetic field (via cyclotron absorption lines and/or spin-down timing) of central objects in a variety of accreting sources, Campana et al. (2018) demonstrated the existence of a universal relation between luminosity, magnetic field, and spin period for the onset of propeller, as theoretically predicted (Equation (2) below), spanning many orders of magnitude in each of these quantities. Their sample included low- and high-mass X-ray binaries (HMXBs), cataclysmic variables, and young stellar objects (YSOs).

Here we select a sample of GRBs that are promising candidates for having a magnetar engine, in that their afterglow light curves show clear evidence for a plateau. Among these, we select only the ones with an accurate estimate of the jet opening angle, and with a prompt emission light curve which is well sampled in time, and has a good spectral coverage to allow an accurate determination of the true bolometric luminosity after correcting for beaming. By measuring the B-field and the spin period from the plateau in the X-ray afterglow, and the transition luminosity from the prompt radiation, we test whether these GRBs verify the same relation as the known accreting sources in propeller. Through this relation we are able to verify the proposed scenario in which accretion energy powers the prompt emission, and the NS spin energy powers the afterglow plateau once accretion subsides. Moreover, we are able to constrain independently the radiative efficiency of accretion in GRBs.

Our paper is organized as follows: Section 2 describes the basics of the theory and the accretor-propeller transition. Section 3 describes the GRB sample, clearly highlighting our selection criteria, and then individually describing the properties of each source. We connect theory to observations in Section 4, where we assess the significance of the correlation that we find. We summarize and conclude in Section 5.

2. The Accretor-Propeller Transition

2.1. General Theory

Matter forming an accretion disk flows toward the accretor by transferring angular momentum outwards, and by releasing (half of) its gravitational potential energy. If the accretor is a magnetic NS (with mass M and radius R), the disk may not reach its surface, being truncated at the magnetospheric radius, $r_m > R$, inside which the NS magnetic field controls the dynamics of the inflowing plasma. In disk geometry r_m is the fraction ξ of the Alfvèn radius, r_A , at which the magnetic pressure balances the ram pressure in a spherical flow (e.g., Pringle & Rees 1972; Frank et al. 2002)

$$r_m = \xi r_{\rm A} = \xi \left(\frac{\mu^4}{2GM\dot{m}^2}\right)^{1/7}.$$
 (1)

Here \dot{m} is the mass accretion rate, $\mu = BR^3/2$ the NS magnetic moment, B the dipole magnetic field at the pole, and the parameter $\xi \sim 0.5$ (e.g., Ghosh & Lamb 1979; Campana et al. 2018) encodes the microphysics of the interaction between the accreting plasma and the B-field corotating with the NS.

When the disk is truncated at $r_m > R$, two cases can occur: (i) if the disk (Keplerian) rotation at r_m is faster than the NS rotation, the NS is in the *accretor* phase, where matter enters the magnetosphere transferring its excess angular momentum to the NS, gradually approaching corotation; (ii) if the disk rotation is slower, the NS enters the *propeller* regime, in which the plasma experiences a centrifugal barrier at r_m and is either flung out (Illarionov & Sunyaev 1975), absorbing in the process some of the stellar angular momentum, or piled up near r_m (e.g., D'Angelo & Spruit 2010).

What differentiates these two cases is the ordering of r_m and of the corotation radius, $r_{\rm co}$, defined as the distance from the NS at which the disk rotation equals the NS angular frequency (ω) , $r_{\rm co} = (GM/\omega^2)^{1/3}$. In the accretor regime, $r_m < r_{\rm co}$, matter falls all the way to the NS surface releasing its remaining gravitational potential energy and producing the accretion luminosity $L = \epsilon GM\dot{m}/R$, where we accounted for a radiative efficiency $(\epsilon \le 1)$. The corresponding, frequently used conversion efficiency of rest mass, η in the relation $L = \eta mc^2$, is $\eta = \epsilon GM/(c^2R)$. In the propeller regime, $r_m > r_{\rm co}$, accretion is halted at r_m and the source has a lower luminosity, $L_{\rm prop} = \epsilon \dot{m} (GM/2r_m)$, at the same mass inflow rate.

The minimum accretion luminosity, L_{\min} , is obtained by first equating r_m to r_{co} : the resulting mass accretion rate, \dot{m}_{\min} , is fed into the expression for L, yielding

$$\log_{10} L_{\min} + \frac{7}{3} \log_{10} P + \log_{10} R_6 = 37.15 + 2 \log_{10} \mu_{30} + \log_{10} \epsilon + \frac{7}{2} \log_{10} \left(\frac{\xi}{0.5}\right) - \frac{2}{3} \log_{10} M_{1.4},$$
(2)

where $Q_x = Q/10^x$ in c.g.s. units, $M_{1.4} = M/(1.4 M_{\odot})$, and $P = 2\pi/\omega$ is the NS spin period (in seconds).

Conversely, the maximum propeller luminosity is obtained by plugging r_{co} and \dot{m}_{min} in the expression of L_{prop}

$$L_{\text{prop}}^{(\text{max})} = \frac{\epsilon \dot{m}_{\text{min}}}{2} (GM\omega)^{2/3} = \frac{\sqrt{2}}{4} \frac{\epsilon \xi^{7/2} \mu^2 \omega^3}{GM}.$$
 (3)

The ratio $L_{\rm min}/L_{\rm prop}^{\rm (max)} \approx 250 M_{1.4}^{1/3} R_6^{-1} P^{2/3}$, depends mainly on the NS spin (Corbet 1996). The corresponding luminosity drop, which is typically used as a signature of the propeller transition, is expected to be small for millisecond spins and smoothed out by the finite time of the transition, thus hardly recognizable in the rapidly variable GRB prompt emission. Theory predicts

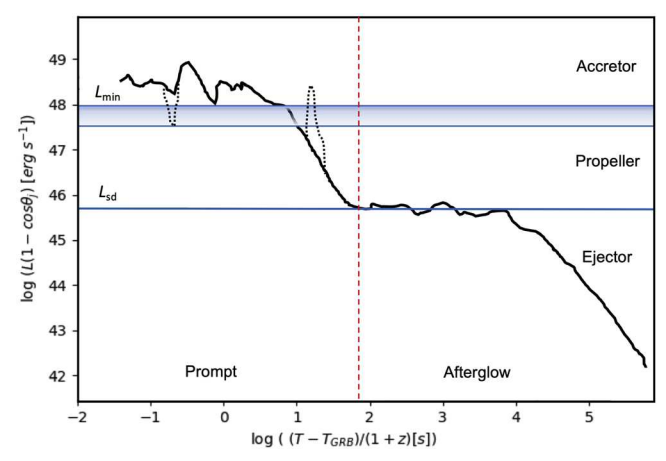


Figure 1. Sketch of a GRB light curve in which an accreting magnetic NS switches from accretion to propeller while in the prompt phase, and then to the ejector regime when the afterglow sets in. The vertical span of the shaded band that separates the accretor from the propeller phase corresponds to the gap between the minimum accretion luminosity, L_{\min} , and the maximum propeller luminosity, $L_{\text{prop}}^{(\text{max})}$. This gap is expected to be small (\sim a few) for millisecond spins. Possible short-term transitions that may take place from the accretion to the propeller regime or vice versa are indicated with a dotted dip or peak in the light curve. The onset of the ejector regime is marked by the early NS spindown luminosity, L_{sd} . Values on the x- and y-axes are roughly indicative of those of (long) GRBs.

another transition, the onset of the so-called "ejector," when the disk edge extends farther out, approaching the light cylinder at $r_L = c/\omega$; then the source luminosity becomes dominated by the NS spin-down, which for ideal magnetic dipole radiation is (Spitkovsky 2006)

$$L_{\rm sd} = \frac{\mu^2}{c^3} \omega^4 (1 + \sin^2 \alpha),$$
 (4)

 α being the angle between the magnetic and rotation axes of the NS. Combining Equations (2) and 4 for $\alpha = \pi/2$ gives the ratio

$$\kappa = L_{\rm min}/L_{\rm sd} \approx 1.2 \times 10^5 \epsilon P^{5/3} (R_6 M_{1.4}^{2/3})^{-1} (\xi/0.5)^{7/2}.$$
 (5)

This ratio too is a function of the NS spin alone⁸ (for given NS mass and radius) but, in contrast to $L_{\min}/L_{\text{prop}}^{(\text{max})}$, it is robustly determined in our case, as the NS spin-down luminosity is well tracked by the luminosity of the afterglow plateau.

2.2. Peculiar Properties of Accretion in GRBs

Figure 1 depicts the light-curve shape expected as a result of the abovementioned transitions. The theory has been developed for and verified in accreting NSs in HMXB Be transients (Stella et al. 1986), low-mass X-ray binaries (LMXBs; Stella et al. 1994; Campana et al. 1998a, 1998b), cataclysmic variables (CVs), and YSOs (Campana et al. 2018), which established the universal character of Equation (2). Compared to such systems, disk accretion in GRBs is expected to present important differences.

In all the sources studied by Campana et al. (2018), the disk material that enters the magnetosphere of the accretor is channeled onto its surface where it releases the gravitational potential energy from r_m to R. The emission we receive comes

from the accretion column, close to the stellar surface, with a typical conversion efficiency of energy to radiation $\epsilon \sim 1$.

In our proposed scenario the GRB prompt emission is still a proxy of the mass accretion rate, yet it comes from shocks in a relativistic jet, much farther away from the central engine. Thus, GRB light curves do not show the characteristic pulsations of accreting NSs signaling their spin periods, and their (featureless) spectra do not offer means for directly measuring the NS *B*-field, in contrast to what occurs in other magnetic accreting stellar objects (e.g., Campana et al. 2018). Furthermore, radiation is believed to come from the conversion of the jet's kinetic energy with an intrinsically low efficiency ($\epsilon_{\gamma} \lesssim 0.1$) and the gravitational potential energy released by accretion is only partially converted into jet kinetic energy ($\epsilon_{\rm jet} < 1$). Thus, it is generally expected that $\epsilon = \epsilon_{\rm jet} \epsilon_{\gamma} \ll 1$.

We will not deal with the details of the interaction between the disk plasma and the millisecond-spinning NS magnetosphere or with the mechanism by which a relativistic jet is launched. We simply assume that the jet will be launched, powered by the energy of accretion and with the known properties of GRB jets, during the accretion phase but not during the propeller regime.

While the relativistic jet carries only a minor amount of baryons, the characteristic mass accretion rate envisioned in the collapsar scenario is $\sim (0.001-1)\,M_\odot\,{\rm s}^{-1}$, implying a total accreting mass $\Delta M \sim (0.001-10)\,M_\odot$ for typical prompt durations $\sim 1-30\,{\rm s}$. Most of the latter may be entrained in a slow-moving and wide outflow or end up onto the NS surface, thus releasing its potential gravitational energy and increasing the NS mass. In this latter case, at the typical GRB mass accretion rates, the infalling material will form a very hot and high-density accretion column in which neutrino emission is dominant (e.g., Piro & Ott 2011; Metzger et al. 2018) while the escaping high-energy radiation is negligible.

Finally, because the maximum gravitational mass allowed by the NS EOS is $M_{\rm g,max}\gtrsim 2.2\,M_\odot$ (Cromartie et al. 2020), the mass increase of the NS may impact its stability against gravitational collapse. In case of core collapse, if the mass of the NS remnant is $\sim 1.4\,M_\odot$, like in the observed NS population (Kiziltan et al. 2013), then there is significant room for accretion before collapse sets in. In short GRBs, on the other hand, the merger remnant is likely to be close to, or above, the maximum NS mass. The probability of a stable NS would depend critically on both the initial component masses in the binary progenitor and the NS EOS (e.g., Dall'Osso et al. 2015; Margalit & Metzger 2017; Piro et al. 2017).

2.3. Main Observables

If the GRB central engine is a millisecond-spinning magnetar, we expect to observe in the prompt light curve the characteristic steep flux decays of switching-off relativistic jets (e.g., Kumar & Zhang 2015) when the NS enters the propeller regime. The minimum accretion flux $F_{\rm min}$, and hence $L_{\rm min}$, can thus be estimated directly from the data (as described in Section 3). Within the magnetar scenario it then becomes possible to verify, in a way that parallels the method of Campana et al. (2018), whether the putative NSs in GRBs follow the universal relation in Equation (2).

Equation (5) assumes the same NS spin at L_{\min} and at the ejector onset.

⁹ See, however, Chirenti et al. (2023).

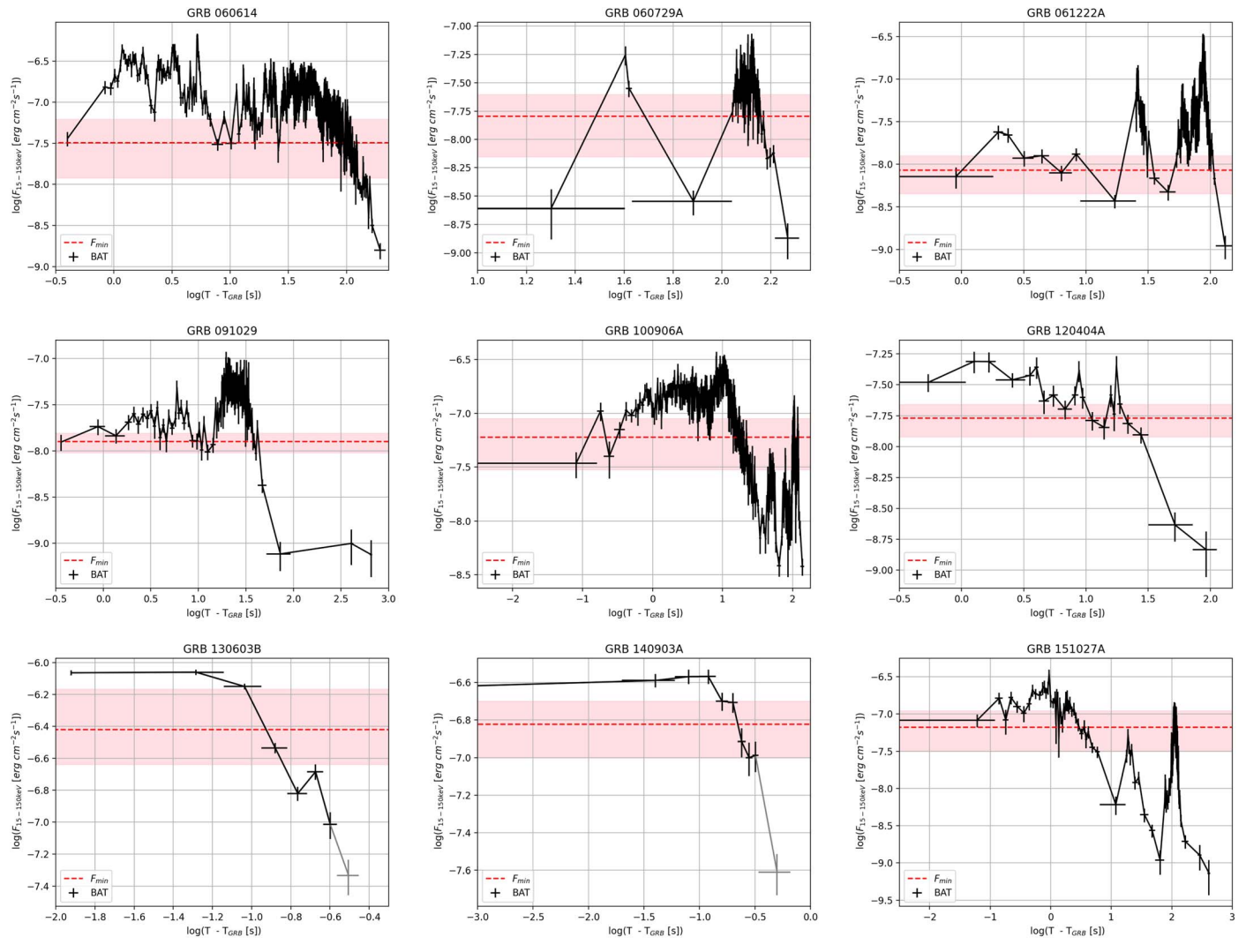


Figure 2. Prompt gamma-ray observed flux light curves from Swift/BAT (15–150 keV) data (with a signal-to-noise ratio of five) for the GRBs in our sample. For each burst, the chosen value of F_{min} is indicated by the red, dashed horizontal line while the pink shaded area indicates the uncertainty on F_{min} , as described in Section 3.1. The gray data points at the end of the two short GRB prompt light curves indicate the flux level obtained from data with a signal-to-noise ratio of four.

With this goal in mind, we searched the prompt light curves of the GRBs in our sample for prolonged and steep flux decays, spanning at least one order of magnitude, in analogy to what is typically done in other classes of accreting compact objects (e.g., Campana et al. 2018 and references therein). Assuming these drops are associated to the propeller onset, we set F_{\min} to be limited by the lowest minimum and the lowest maximum prior to the flux decay or by the occurrence, after the decay, of a new peak signaling a new temporary transition to the accretor phase. With these criteria we defined an allowed range for F_{\min} , and set the fiducial values at the midpoint of the range. In Section 3 we provide more details on this procedure for each GRB. Our results, illustrated in Figure 2, are reported in Table 2. Moreover we estimated the NS spin period P at the end of the prompt phase, and its magnetic dipole field strength B by fitting the observed plateau in the X-ray afterglow with a model of energy injection by a spinning down magnetar, as further discussed in Section 3.3 (see Dall'Osso et al. 2011; Bernardini et al. 2013; Stratta et al. 2018).

Note that here we estimate L_{\min} directly from the prompt light curve, independently of the B- and P-values derived from

the afterglow, whereas Bernardini et al. (2013) used the latter values to infer L_{\min} in the prompt phase. Ultimately, this allows us to verify the validity of Equation (2) using independent quantities, while at the same time constraining the radiative efficiency, $\epsilon = \epsilon_{\rm jet} \epsilon_{\gamma}$.

3. Data Analysis

We selected a sample of both long and short GRBs detected with the Swift satellite and at known distances that present (i) clear evidence of an X-ray plateau in the afterglow light curve, (ii) a well-sampled prompt emission light curve, to allow the study of flux variations consistent with transitions to the propeller phase, (iii) a good spectral coverage of the prompt emission with a measure of the peak energy, and (iv) an accurate estimate of the jet opening angle θ_j from multiband afterglow data. Meeting these four criteria is challenging. For this reason, the resulting sample is made of only nine events, two of which are short GRBs (140903A and 130603B; see Table 1).

Table 1
Prompt Emission Properties taken from the Swift–Konus/Wind GRB Catalog (Tsvetova et al. 2017, 2020) for the GRBs of our sample

GRB	z	T _{90,100} (s)	F(E)	E _{peak,obs} (keV)	α	β	K	$E_{\text{iso,51}}$ 1/(1+z) keV-10 MeV
091029	2.75	50	BAND	66	-1.56	-2.38	2.39	156.5
100906A	1.73	90	CPL	195	-1.6		2.54	249
151027A	0.81	117	CPL	173	-1.44		2.23	33.0
061222A	2.09	60	CPL	298	-0.89		2.95	259.9
120404A	2.88	43	CPL	70	-1.61		2.09	103.1
060729A	0.54	126	BAND	8.7	-1.14	-2.05	2.94	58
060614	0.13	123.6	CPL	76	-1.92	•••	2.82	2.7
130603B	0.36	0.07	CPL	607	-0.67	•••	6.64	1.96
140903A ^a	0.35	0.3	BAND	40	-1	-2	3.14	0.06

Notes. The best-fit prompt emission spectral model F(E) is taken as the one corresponding to the integrated spectrum (flag "i"), where BAND is the Band model (Band et al. 1993) and CPL is the cutoff power-law model with cutoff energy $E_{\rm cut} = E_{\rm peak}/(2+\alpha)$ and α is the power-law photon index. The last two lines indicate the two short GRBs present in our sample.

 Table 2

 Selected Sample of Nine GRBs Analyzed in This Work

GRB	θ_j (rad)	$F_{\text{min}, 15-150 \text{ keV}} $ (10^{-7} cgs)	$L_{\text{min}, 1-10^4 \text{ keV}} $ $(10^{47} \text{ erg s}^{-1})$	P (ms)	$^{B}_{(10^{14} \text{ G})}$	ϵ	$L_{p,X,0.3-30 \text{ keV}} $ (10 ⁴⁴ erg s ⁻¹)	$\epsilon_{ m sd}$
060614	0.18	$0.32^{+0.3}_{-0.2}$	$0.6^{+0.7}_{-0.5}$	30.3 ± 0.5	50.3 ± 1.9	$0.07^{+0.10}_{-0.07}$	0.08 ± 0.04	0.17 ± 0.04
060729A	$0.114^{+0.004}_{-0.004}$	$0.16^{+0.09}_{-0.09}$	$3.5^{+2.0}_{-2.0}$	2.90 ± 0.03	4.63 ± 0.08	$0.23^{+0.14}_{-0.14}$	2.6 ± 0.2	0.16 ± 0.04
061222A	$0.0684^{+0.014}_{-0.006}$	$0.08^{+0.04}_{-0.04}$	$18.8^{+10.0}_{-12.0}$	0.87 ± 0.02	7.01 ± 0.35	$0.03^{+0.02}_{-0.02}$	500 ± 200	0.27 ± 0.07
091029	$0.022^{+0.016}_{-0.016}$	$0.13^{+0.03}_{-0.03}$	$7.0^{+3.7}_{-3.7}$	1.54 ± 0.09	9.5 ± 0.5	$0.024^{+0.01}_{-0.01}$	6.0 ± 3.8	0.17 ± 0.06
100906A	0.05	$0.6^{+0.3}_{-0.3}$	38^{+33}_{-27}	1.72 ± 0.07	16.2 ± 0.9	$0.06^{+0.05}_{-0.05}$	110 ± 70	0.34 ± 0.09
120404A	$0.0541^{+0.005}_{-0.005}$	$0.17^{+0.05}_{-0.05}$	36^{+13}_{-13}	2.54 ± 0.23	34.1 ± 1.8	$0.03^{+0.01}_{-0.01}$	43 ± 9	0.12 ± 0.05
130603B	$0.11^{+0.03}_{-0.09}$	$3.8^{+3.0}_{-1.5}$	126^{+110}_{-67}	13.3 ± 1.1	153 ± 11	$0.26^{+0.25}_{-0.16}$	8.7 ± 3.6	0.22 ± 0.09
140903A	$0.07^{+0.09}_{-0.03}$	$1.5^{+0.5}_{-0.5}$	$5.1^{+2.9}_{-2.9}$	13.7 ± 1.5	39 ± 5	$0.17^{+0.13}_{-0.13}$	0.3 ± 0.2	0.32 ± 0.16
151027A	0.11	$0.66^{+0.44}_{-0.34}$	28^{+26}_{-20}	2.00 ± 0.01	12.7 ± 0.2	$0.10^{+0.10}_{-0.08}$	150 ± 90	0.29 ± 0.04

Note. The magnetar energy output is assumed to be emitted isotropically and the NS angular momentum is assumed to be orthogonal to the magnetic axis. The second column gives the jet opening angle, while the third and fourth columns respectively quote the minimum flux (Swift/BAT) and corresponding (bolometric) luminosity in the prompt phase before the NS enters the propeller regime. P and B are the magnetar spin period and dipole B-field strength obtained by fitting the X-ray afterglow light curves, respectively, and ϵ is the conversion efficiency from gravitational potential energy to γ -rays. The eighth column quotes the (beaming-corrected) plateau luminosity in the earliest time bin, while the last column reports the inferred conversion efficiency from NS spin-down power to plateau luminosity.

3.1. Estimating F_{\min}

To estimate the minimum flux level $F_{\rm min}$ associated with the accretion phase, we used the publicly available Swift/BAT 15–150 keV prompt light curves with temporal resolution that guarantees a signal-to-noise ratio > 5. Following Section 2.3, for each prompt light curve, we identified a maximum and minimum flux within which we could confidently constrain the propeller transition. Specifically, the maximum flux was associated with the faintest of the peaks that characterize the bright prompt phase, while the minimum flux with minima prior to the steep flux decrease. Results are quoted in Table 2.

Below we describe, for each GRB, the prompt emission features based on which we estimate F_{\min} , as well as the studies from which the θ_i -values were adopted.

3.1.1. GRB 060614

This peculiar GRB at z = 0.125 has a duration, $T_{90} = 102$ s, suggesting a long GRB classification, while the lack of an associated supernova down to very deep limits, and its

location in the time-lag-peak-luminosity plane, are more consistent with the properties of short GRBs (Mangano et al. 2007).

The prompt emission light curve is very well sampled, the X-ray afterglow has a clear plateau and an excellent multiband data set is also available. The jet opening angle was taken from Mangano et al. (2007) that quote $\sim\!10^\circ\!.5$ from a very robust achromatic temporal break observed in the afterglow light curve 117 ks after the burst onset.

The prompt light curve shows two bright intervals separated by a hollow minimum at $\lesssim 10$ s. Starting at ~ 50 s posttrigger, an extended and steep flux decay is observed. Prior to it, the hollow minimum and the lowest peak at $\lesssim 10$ s indicate a narrow range of possible $F_{\rm min}$ -values, consistent with the flux in the first part of the steep decay. We extended this range to include even the lowest peak at $\gtrsim 100$ s, a choice that has only a minor effect on the fiducial value of $F_{\rm min}$.

3.1.2. GRB 060729A

The Swift/BAT light curve of this GRB, at z = 0.543, shows clear evidence of a precursor followed by a long quiescence

^a GRB 140903A is the only one not present in the Swift-Konus/Wind catalog and we assumed a BAND model with fiducial values (see text).

¹⁰ From the Swift/XRT Burst Analyzer repository (Evans et al. 2010).

time (\sim 100 s), which is ended by a typical burst lasting \sim 40 s. The X-ray light curve of its afterglow is characterized by a long plateau 11 (\gtrsim 4 × 10⁴ s) and postplateau power-law decay, with a very late break (Racusin et al. 2009). From the X-ray light curve alone (see Cano et al. 2011 for a detailed study of optical data from different instruments) these authors classified GRB 060729A as a "prominent jet-break" case, and measured its θ_j accounting for the effect of prolonged energy injection, which may extend the power-law decay beyond the time expected in the standard scenario. Given the accurate determination of $\theta_j = 6.5^{+0.25}_{-0.15}$, we included this event in our sample.

The F_{min} -range in this GRB is constrained between the lowest peak at $\approx 160 \text{ s}$ and the flux at the onset of the steep flux decay; the latter feature appears to be repeated twice in the Swift/BAT light curve (upper central panel in Figure 2).

3.1.3. GRB 061222A

This is the brightest long GRB in our sample. Its light curve was recognized by Bernardini et al. (2013) as a prototypical example of the way in which the propeller mechanism can switch a GRB central engine on and off. The prompt phase, lasting $\sim\!150\,\mathrm{s}$, is characterized by three main pulses of which the latest is the brightest. We identified F_{min} as being constrained between the lowest peaks and the lowest minima observed prior to the steep flux decays occurring at $\lesssim\!30\,\mathrm{s}$ and at $\lesssim\!100\,\mathrm{s}$.

A half-opening angle \sim 2°.4 was inferred, like for GRB 100906A, in the multiband afterglow analysis by Chandra & Frail (2012). The more recent and detailed study by Ryan et al. (2015) quoted a similar result, providing $\theta_j = 3^{\circ}.7^{+0.8}_{-0.4}$, the value adopted here.

3.1.4. GRB 091029

This bright long burst has a prompt duration $T_{90} = (39 \pm 5) \, \mathrm{s}$ in the Swift/BAT range (Barthelmy et al. 2009). At $\sim \! 35 \, \mathrm{s}$ we identify the characteristic flux drop indicating the onset of the propeller regime. Comparing with the lowest peaks and minima prior to this transition (in particular at $T - T_{\mathrm{obs}} < 10 \, \mathrm{s}$), we determined a narrow range for F_{min} with a central value of $F_{\mathrm{min}} \approx 1.3 \times 10^{-8} \, \mathrm{erg \, cm^{-2} \, s^{-1}}$.

The afterglow of this GRB was monitored in several bands (e.g., Filgas et al. 2012). The optical light curve shows a few rebrightenings that challenge the measure of the jet-break epoch in this band. Lu et al. (2012) determined $\theta_j \sim 0.058$ rad (\sim 3°.3) in a Swift GRB sample study on the selection effects in the apparent $\theta_j - z$ dependence. Ryan et al. (2015) obtained $\theta_j = 12^{+11}_{-8}$ deg, and a viewing angle $\theta_v = 0.75^{+0.18}_{-0.47} \times \theta_j$, modeling the X-ray afterglow by means of a high-resolution hydrodynamical model with no angular structure in the jet (top hat), and imposing a narrow prior on $\theta_j \sim [2^\circ.6-28^\circ.6]$.

By studying the optical/X-ray afterglows of a sample of GRBs, Wang et al. (2018) identified an achromatic temporal break at (30.0 \pm 6.8) ks for this burst. By assuming a constant density circumburst medium (ISM), and the standard jet-break formula (e.g., Equation (1) in Sari et al. 1999), a half-opening angle $\theta_j = 1.24 \pm 0.92$ was inferred. Here we adopt this latter result, which was obtained from the identification of an achromatic break in a multiband study.

3.1.5. GRB 100906A

This is a long GRB among the brightest of our sample. Its Swift/BAT prompt duration is $T_{90} = (114.4 \pm 1.6)$ s (Barthelmy et al. 2010) and its light curve shows a main bursting episode followed by a flux decay and then by multiple lower peaks (Figure 2). The steep flux decay at $t \approx (10-30)$ s marks the onset of the propeller regime, from which we estimate a fiducial value of $F_{\rm min} \sim 6 \times 10^{-8}$ erg cm⁻²s⁻¹, further supported by the later peaks, at $t \approx 120$ s, reaching a similar flux.

The jet half-opening angle $\theta_j = 2^{\circ}.9$ for this burst is taken from the multiband afterglow study by Chandra & Frail (2012), who assumed a constant density circumburst environment following Sari et al. (1999).

3.1.6. GRB 120404A

The prompt duration of this long GRB is $38.7 \pm 4.1 \, \mathrm{s}$ in the $15{\text -}150 \, \mathrm{keV} \, \mathrm{Swift/BAT}$ band (Ukwatta et al. 2012). The light curve shows mildly fluctuating flux up to $\sim\!20 \, \mathrm{s}$, when a steep flux decay begins. Peaks and dips in the early $20 \, \mathrm{s}$ constrain F_{min} in a range that is perfectly consistent with the turning point of the flux decay at $F_{\mathrm{min}} \approx 2 \times 10^{-8} \, \mathrm{erg} \, \mathrm{cm}^{-2} \, \mathrm{s}^{-1}$.

Guidorzi et al. (2014) measured $\theta_j \sim 23^{\circ}$ fitting broadband, high-quality optical/NIR data with the hydrodynamical code of Van Eerten et al. (2012). Their fit, which did not include energy injection, was found to underpredict the X-ray flux compared to the optical, and required a very steep power-law slope of $p \sim 3.4$ for the electron energy distribution.

Laskar et al. (2015) described the broadband afterglow light curve (radio, NIR, optical, and X-rays) with a phenomenological energy injection model. They obtained $\theta_j = 3.1 \pm 0.3$ and $p \approx 2.1$, interpreting the optical/X-ray decline $\sim t^{-2}$ seen at ~ 0.1 day as indicative of a jet break. For these reasons we adopt in the following this latter value of θ_i .

3.1.7. GRB 130603B

For this short GRB at z=0.36 a kilonova component was identified in the optical/NIR afterglow \sim one week after the event (Tanvir et al. 2013), consistent with a binary NS merger. The possible range of $F_{\rm min}$ is limited from above by the flux at the onset of the steep flux decay, at $T-T_{\rm obs}\approx 0.085$ s, and from below by the occurrence of a late peak at $T-T_{\rm obs}\approx 0.2$ s. Accordingly, we determined a fiducial value $F_{\rm min}\approx 3.8\times 10^{-7}$ erg cm $^{-2}$ s $^{-1}$.

The jet half-opening angle was measured from multiband jet-break observations as $\theta_j \sim 4^\circ - 8^\circ$ assuming a constant density circumburst medium with n < 1 cm⁻³ (Fong et al. 2015). Adopting the same method and setting n = 1 cm⁻³, Wang et al. (2018) obtained $\theta_j = (4^\circ.47 \pm 0^\circ.68)$.

Recently, the afterglow light curve was reanalyzed by Aksulu et al. (2022) by means of ScaleFit hydrodynamical simulations (Ryan et al. 2015), obtaining $\log \theta_j = -0.97^{+0.28}_{-0.54}$, i.e., $\theta_j = 6.3^{+1.7}_{-5.1}$. In this work we assume the latter result.

3.1.8. GRB 140903A

This short GRB is more than 20 times less energetic than the other one in our sample (GRB 130603B) and at a similar redshift (z = 0.35). Its Swift/BAT light curve is roughly constant, with minor fluctuations, up to about $\lesssim 0.3$ s, after which it decays close to the detection limit. We interpret the early behavior as being due

¹¹ Incidentally, a NASA press release of this burst highlighted its peculiar plateau, suggesting a magnetar central engine https://www.nasa.gov/centers/goddard/news/topstory/2007/gammaburst_challenge.html.

to accretion at various luminosity levels, and the later decay as due to the onset of propeller. Accordingly, we set $F_{\rm min}$ at $\approx 1.5 \times 10^{-7}$ erg cm⁻² s⁻¹.

There are no Konus/Wind data for this burst. However, its Swift/BAT 15–150 keV spectrum is consistent with a power law $F(E) \propto E^{-\Gamma}$, with photon index $\Gamma = 1.99 \pm 0.08$ (Troja et al. 2016). The relation $\log(E_{\rm peak}) = 3.258$ –0.829 Γ , for $1.3 < \Gamma < 2.3$ (Sakamoto et al. 2009), can thus be used to derive a rough estimate of the peak energy. Accordingly, we assumed a Band model (Band et al. 1993) with observed peak energy \sim 40 keV, and spectral indices $\alpha = -1$ and $\beta = -2$.

The multiband afterglow monitoring shows indications for an achromatic break at $t \sim 10^5$ s (Troja et al. 2016). Using the hydrodynamic simulations of van Eerten (2015), the multiband data fitting by Troja et al. (2016) determined a jet half-opening angle $\theta_j = 5^{\circ}.0 \pm 0^{\circ}.7$. A consistent value, $4^{\circ}.0^{+5.0}_{-1.6}$, was determined by Aksulu et al. (2022) using a different set of hydrodynamical simulations of structured jets. Here we adopt the latter, more recent result.

3.1.9. GRB 151027A

The duration of this long GRB derived from its Swift/BAT light curve is 130 ± 6 s (Palmer et al. 2015). The bright peak in the first ~ 3 s is followed by a steep decay up to ~ 10 s, and then by a minor rebrightening between ~ 15 and ~ 25 s, where it reaches a peak $\sim 30\%$ of the one at 3 s. About ~ 60 s after the burst trigger the light curve shows a new substantial flux increase, strongly suggestive of a new temporary onset of accretion. This interpretation is supported by the flux level reached in this second bright episode, which is comparable to the one at ~ 3 s. Therefore, we adopt the flux measured at 3 s as $F_{\rm min}$, with a value of $\approx 6.6 \times 10^{-8}$ erg cm⁻² s⁻¹.

A comprehensive multiband study of this bust was carried out assuming a wind environment, as suggested by late radio data, deriving $\theta_i \sim 6^{\circ}.3$ (Nappo et al. 2017).

3.2. Determination of L_{min}

We proceed to compute the $1-10^4$ keV minimum luminosity L_{min} of each GRB as

$$L_{\min} = KF_{\min} 4\pi D_L^2 f_b, \tag{6}$$

where $f_b = (1 - \cos \theta_j)$ is the beaming factor and D_L is the luminosity distance. The *K*-correction converts the (15–150) keV observed fluxes to the (1–10⁴) keV rest-frame ones

$$K = \frac{\int_{1 \text{ keV}/(1+z)}^{10^4 \text{keV}/(1+z)} F(E) dE}{\int_{15 \text{ keV}}^{150 \text{ keV}} F(E) dE},$$
(7)

where F(E) is the prompt emission best-fit spectral model¹², taken from the joint Konus/Wind (20 keV-15 MeV) and Swift/BAT (15–150 keV) GRB catalogs¹³ (Tsvetkova et al. 2017, 2021). Table 1 reports the adopted spectral model and its parameters, the observed prompt peak energy E_p , and the isotropic-equivalent energy $E_{\rm iso}$ in the $(1-10^4)/(1+z)$ keV band from the same catalog.

The uncertainty on L_{\min} includes the one on the jet opening angle as well as the uncertainty inherent in the adopted value of F_{\min} , and is computed as

$$dL_{\min} = K4\pi D_L^2 \sqrt{[(f_b dF_{\min})^2 + (F_{\min} df_b)^2]}.$$
 (8)

Here we adopted $df_b \approx \sin\theta_j d\theta_j$ if $d\theta_j < 0.5 \, \theta_j$, otherwise $df_b = (f_{b,\text{max}} - f_{b,\text{min}})/2$ where $f_{b,\text{max}}$ and $f_{b,\text{min}}$ are the collimation factors corresponding to $\theta_j + d\theta_j$ and $\theta_j - d\theta_j$, respectively. When θ_j is provided in the literature without an error, we assume a conservative $d\theta_j = 0.5\theta_j$ and apply the latter formula. In general, we find that both the uncertainties on θ_j and on F_{min} contribute significantly to the resulting uncertainties in L_{min} .

3.3. Parameter Estimation for Magnetars

To estimate the NS B-field and spin period we fit the X-ray afterglow plateaus with the model of energy injection from a spinning down magnetar developed by Dall'Osso et al. (2011) and further generalized in Stratta et al. (2018). In the model, the plateau luminosity (L_p) and duration (T_p) are proxies of the same quantities in the magnetar spin-down law, which in turn are determined by B and P (e.g., Figure 1 in Dall'Osso et al. 2011). In particular, a straightforward interpretation of fit results is enabled by use of the standard approximations (e.g., Dall'Osso & Stella 2022)

$$T_p \sim 6.8 \times 10^4 \left(\frac{P_{\rm ms}}{B_{14}}\right)^2 {
m s}$$

$$L_p(t) \sim \epsilon_{\rm sd} \frac{E_{\rm spin,i}}{T_p} \left(1 + \frac{t}{T_p}\right)^{-2}, \qquad (9)$$

where B_{14} is the NS dipole magnetic field in units of 10^{14} G, $P_{\rm ms}$ is the initial spin period in milliseconds, $E_{\rm spin,i}$ is the initial spin energy, and we added $\epsilon_{\rm sd}$, the conversion efficiency from the NS spin-down power to afterglow X-ray emission.

break;ray luminosity is computed as $L_{p,X}(t) = K'F_X(t)4\pi D_L^2 f_b$, where the X-ray flux $F_X(t)$ is taken from the Swift/XRT Burst Analyzer repository (corrected for absorption; see Evans et al. 2010). Here the K-correction converts from the observed (0.3–10) keV band to the rest-frame (0.3–30) keV band. The beaming factor f_b is the same as that adopted for the prompt emission in Equation (6) (see Table 2).

The magnetar luminosity is assumed to be released isotropically during the plateau, as typically done in the literature (e.g., Rowlinson et al. 2013; Piro et al. 2019). Consequently, in order to calculate the rate of energy injection in the external shock, the luminosity $L_{\rm sd}$ was reduced by the fraction of solid angle intercepted by the GRB jet, i.e., the beaming factor f_b . Figure 3 shows the beaming-corrected afterglow light curves of the nine GRBs in our sample in the 0.3–30 keV rest-frame energy range. Superposed are the best-fit energy injection models. The best-fit B and P values are reported in Table 2.

4. Results: Connecting Theory to the Data

With the derived values of $L_{\rm min}$, B and P, reported in Table 2, each GRB is plotted in the $L_{\rm min}P^{7/3}R_6$ versus μ plane, for an NS radius of 12 km, in order to test their consistency with the universal relation (Equation (2)).

Best-fit models refer to the GRB integrated spectra rather than the peaks.

¹³ GRB 140903 is the only event not present in these catalogs. Its spectral model is discussed in Section 3.1.8.

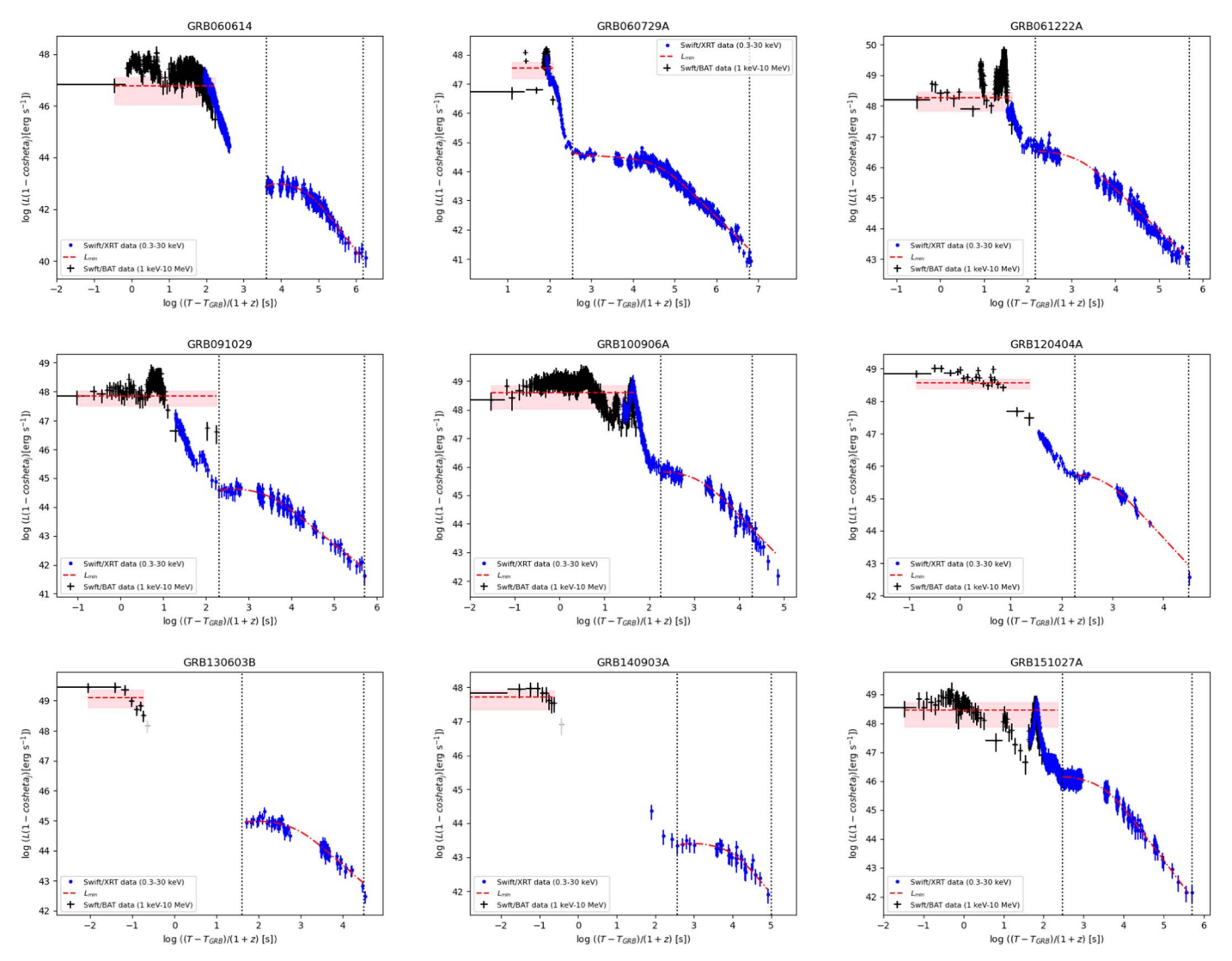


Figure 3. GRB prompt and afterglow luminosity light curves in the (1 keV-10 MeV) and (0.3-30 keV) rest-frame energy range, respectively. The luminosity is corrected for jet beaming. Black vertical dotted lines indicate the temporal window considered for the magnetar model fit. Red dashed–dotted lines indicate, for each GRB, the best-fit magnetar model from which we obtain the magnetic field strength B and spin period P (see Table 2). Horizontal dashed red lines mark the minimum accretion luminosity (L_{\min}) before entering the propeller regime, and the pink shading shows the uncertainty on L_{\min} . The latter is wider than the uncertainty on F_{\min} (Figure 2), due to the added uncertainty on the beaming factor (f_b).

4.1. Universal Relation

We find a strong correlation for the GRBs in our sample in the $\log_{10}(L_{\min}P^{7/3}R_6)$ versus $\log_{10}\mu_{30}$ plane, with a Pearson correlation coefficient r=0.948 and two-tailed p-value $=9.7\times10^{-5}$. If we discard the two short GRBs (GRB 130603B and GRB 140903A), for which L_{\min} is more uncertain, the correlation remains significant, r=0.891 and p-value =0.007. The correlation has the form 14 $y=(2.3\pm0.3)$ $x+(35\pm1)$ in the plane of Figure 4; the slope is consistent, within the uncertainties, with the one expected from theory (Equation (2)) and observationally confirmed by Campana et al. (2018) for other types of accretion-powered sources hosting a magnetic stellar object, $y=2x+(37.12\pm0.20)$ with $\xi=0.5$ and $\epsilon=1$. Compared to the latter, the GRBs in our sample require a lower normalization, which is readily interpreted in terms of a reduced radiative efficiency of their

gravitational potential energy to prompt radiation (ϵ) is expected to be low in GRB disks. From Equation (2) we estimate for each GRB the value of 15 ϵ implied by its position in the plane of Figure 4

central engines (Equation (2)), as predicted by theory. Indeed, as discussed in Section 2.2, the efficiency of conversion of

$$\log_{10} \epsilon = \log_{10} y - 2\log_{10} \mu_{30} - \frac{7}{2}\log_{10} \left(\frac{\xi}{0.5}\right) - 37.15 \quad (10)$$

and derive typical values of $\epsilon \sim (0.03-0.26)$, as reported in Table 2. The corresponding conversion efficiencies from rest mass to prompt radiation, $\eta \sim (0.5-4) \times 10^{-2} M_{1.4} R_6^{-1}$, are remarkably consistent with the range estimated from an analysis of GRB prompt and afterglow light curves (e.g., Zhang et al. 2007), with the two short GRBs in the sample requiring the largest efficiencies.

¹⁴ It is $y = (1.8 \pm 0.3)x + (36.2 \pm 1.2)$ if we remove the two short GRBs.

In Equation (10) we omit for simplicity the dependence on $M_{1.4}^{2/3}$.

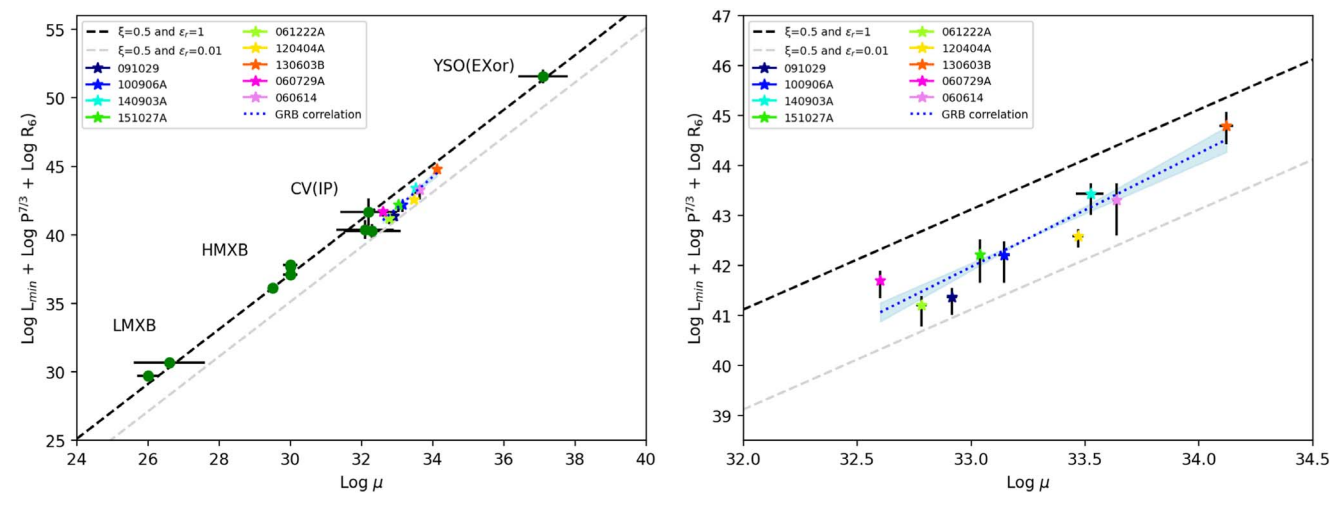


Figure 4. Left: the universal relation for two different radiative efficiencies, $\epsilon=1$ (dashed thick line) and $\epsilon=0.01$ (dashed light-gray line; see Equation (2)). Green dots indicate different classes of accreting compact objects studied by Campana et al. (2018). Colored stars are the GRBs analyzed in this work and for which an isotropically radiating magnetar central engine is assumed. The blue dotted line is the best-fit correlation for the nine GRBs, with a Pearsons correlation coefficient = 0.948 corresponding to a two-tailed p-value for testing a noncorrelation of 9.7×10^{-5} . Right: close-up of the left panel, highlighting the GRB population alone. The shaded area around the correlation (blue dotted line) shows the uncertainty in the fit parameters.

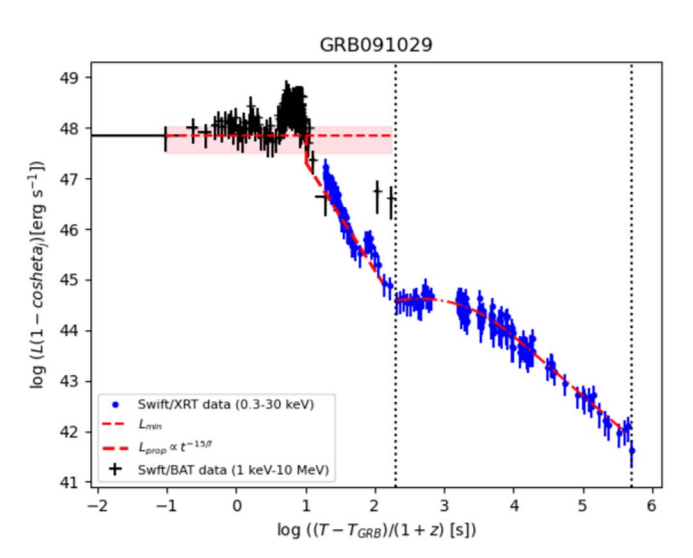


Figure 5. GRB 091029 light curve from the prompt phase to the end of the plateau. The red dotted—dashed curve shows our model prediction for the minimum accretion luminosity, L_{\min} , the propeller luminosity, the switch on time for the ejector phase $(r_m = r_L)$ and the plateau luminosity. Note that this is not a fit, but the curve expected given (L_{\min}, B, P) .

Factors like the mass and radius of each individual NS may contribute to the scatter of the correlation; a more crucial role in Equations (2) and (10) may be played by the ξ -value. Campana et al. (2018) showed that the data point to $\xi \approx 0.5$ in their composite sample of sub-Eddington sources. We note that, if $\xi \approx 1$, as some authors suggest for very high accretion rates (e.g., Andersson et al. 2005; Kulkarni & Romanova 2013), then the estimated ϵ in Equation (10) could be further reduced by up to a factor $\lesssim 10$.

4.2. Testing the Energy Source: Disk Accretion and NS Spin

We further corroborate this scenario by showing that, for each GRB, the accretion luminosity L_{\min} in the prompt phase and the afterglow luminosity at the onset of the plateau (as measured in its first temporal bin) satisfy the theoretically expected value (Equation (5)), once the accretion radiative

efficiency (ϵ) for that GRB is factored in. To this aim we calculate, for each GRB in our sample, the ratio $L_{\min}/L_{p,\mathrm{iso}} = L_{\min}/(\epsilon_{\mathrm{sd}}L_{\mathrm{sd}}) = \kappa/\epsilon_{\mathrm{sd}}$ using the L_{\min} -values from the previous section and the isotropic-equivalent plateau luminosity, $L_{p,\mathrm{iso}} = \epsilon_{\mathrm{sd}}L_{\mathrm{sd}}$, as a proxy for the NS spin-down power. As in Equation (9), we include the efficiency ϵ_{sd} to allow for imperfect conversion of the spin-down power into plateau emission. We then equate the observationally determined $L_{\min}/L_{p,\mathrm{iso}}$ to its expected value (see Equation (5)), $\kappa/\epsilon_{\mathrm{sd}} \approx 10^5 \ \epsilon/\epsilon_{\mathrm{sd}} P^{5/3} (\xi/0.5)^{7/2}$ (for $R=12 \ \mathrm{km}$ and $M=1.4 \ M_{\odot}$) and derive the ratio $\epsilon/\epsilon_{\mathrm{sd}}$. For each GRB, Table 2 reports the resulting value of ϵ_{sd} adopting the best-fit spin period from the plateau and the ϵ derived from Equation (10). We obtain typical values of $\epsilon_{\mathrm{sd}} \sim 0.12-0.34$, remarkably similar for all the GRBs in our sample, confirming within the uncertainties the self-consistency of the proposed

Note that, if the spin-down were enhanced by a factor β relative to the ideal magnetic dipole formula of Equation (4) (e.g., Parfrey et al. 2016; Metzger et al. 2018), then a somewhat lower $\epsilon_{\rm sd}/\beta$ would result. In addition, our results would be weakly affected even if the magnetar wind, responsible for energy injection, were mildly beamed, e.g., by a factor $f_w > 0.14$ (i.e., $\theta_w > 30^\circ$) along the jet axis. At a fixed jet halfopening θ_i , beaming of the magnetar wind would imply that a larger fraction of its spin-down power is intercepted by the jet, relative to an isotropic wind. Thus, the required luminosity of the magnetar would also be lower by a factor f_w . We have verified that, as a result of this change, each point in Figure 4 will shift toward regions of slightly lower radiative efficiency. In particular, ϵ would be reduced by just $f_w^{1/6}$, while $\epsilon_{\rm sd}$ would increase by $f_w^{-2/3}$, relative to our fiducial values in Table 2.

4.3. Propeller, Ejector, and NS Dynamics

At time T_{\min} the prompt luminosity drops below L_{\min} and the NS enters the propeller regime. Here the interaction of the magnetosphere with the (slower) material in the Keplerian disk causes a phase of enhanced spin-down with respect to

Equation (4). This phase will end only when the NS switches to the ejector regime, in which the disk is expelled from the magnetosphere (as its inner edge approaches the light cylinder) and the NS spins down due to magnetic dipole radiation (Equation (4)). As a result the spin period P estimated from the plateau may be longer than $P(T_{\min})$, i.e., the spin period at time T_{\min} . Moreover, the luminosity evolution from T_{\min} through $T_{\rm pl}$, the plateau start time, will track the power released in the disk down to r_m . We check here the consistency of observed GRB light curves with the above expectations. A more systematic study of light-curve shapes as a function of model parameters is deferred for future investigation.

Our first step is to check the impact of propeller-induced spin-down on the NS rotation from T_{\min} to $T_{\rm pl}$. For each GRB we estimate $\dot{m}_{\min} = L_{\min}R/(GM\epsilon)$ at time T_{\min} , and the corresponding $r_m(T_{\min})$. However, we do not use here the previously calculated radiative efficiency since, as Equation (10) shows, $\epsilon \sim L_{\min}RP(T_{\min})^{7/3}/(\mu^2\xi^{7/2})$; thus ϵ , \dot{m}_{\min} , and $r_m(T_{\min})$ will all depend on the unknown $P(T_{\min})$.

For the mass inflow rate during the propeller phase we adopt the standard scaling $\dot{m} \propto t^{-5/3}$ for fallback (e.g., Rees 1988; MacFadyen & Woosley 1999), and the accretion power released in the disk while in propeller $L_{\rm prop}(t) = \epsilon GM\dot{m}(t)/2r_m(t)$. Writing $\dot{m}(t) = \dot{m}_{\rm min}(t/T_{\rm min})^{-5/3}$, and using $r_m \propto \dot{m}^{-2/7}$ (Equation (1)), we get

$$L_{\text{prop},47}(t) \approx 0.8 \frac{M_{1.4}^{8/7} \epsilon_{-2} \dot{m}_{min,-4}^{9/7}}{(\xi/0.5) \mu_{33}^{4/7}} (t/T_{min})^{-15/7}, \tag{11}$$

with $\dot{m}_{\rm min,-4} = \dot{m}_{\rm min}/(10^{-4} M_{\odot}/{\rm s})$ and $\mu_{33} = \mu/(10^{33} \,{\rm G\,cm}^3)$. The maximum rate of angular momentum transfer from the

The maximum rate of angular momentum transfer from the NS to disk material is (e.g., Piro & Ott 2011; Parfrey et al. 2016; Metzger et al. 2018) $\dot{J}_{\text{prop}}(t) = \dot{m}(t)\omega(t)r_m(t)^2 = -I\dot{\omega}(t)$, from which we obtain the evolution of the NS spin frequency

$$\omega(t) = \omega(T_{\min}) \exp\left[-\frac{\int_{T_{\min}}^{t} \dot{m}(t') r_m^2(t') dt'}{I}\right]. \tag{12}$$

After some manipulation the integrand in Equation (12) becomes

$$\dot{m}(t)r_m^2(t) = \frac{\pi\sqrt{2}\,\xi^{7/2}\mu^2}{GMP(T_{\rm min})}(t/T_{\rm min})^{-5/7}\,,\tag{13}$$

which is solved for $P(T_{\min})$ once we determine the start time of the plateau $(T_{\rm pl})$ and impose that $P(T_{\rm pl})$ equals the best-fit value P from Table 2. Thus, for each GRB in our sample we first estimated T_{\min} and $T_{\rm pl}$ from the light curves, and then solved Equation (12) for $P(T_{\min})$. We show in Table 3 the resulting $P(T_{\min})$ for each GRB in our sample, along with the values of T_{\min} , $T_{\rm pl}$, and the implied \dot{m}_{\min} . In all but one case the spin change is small or negligible, compared to the fit error, and the same holds for the ϵ -value. Only GRB 060614 requires a \sim 2 times faster spin at T_{\min} owing to its longer initial spin period, which leads to a prolonged propeller phase.

This result fully supports the robustness of the universal relation, and its interpretation discussed in the previous sections¹⁷.

Moreover, the proposed scenario provides us with a simple self-contained model for GRB light curves from the onset of the prompt steep decay to the end of the afterglow plateau, which depends only on three parameters: $L_{\rm min}$, B, and P. As an example, we show in Figure 5 the application of this model to the light curve of GRB 091029: having determined B and P from the afterglow plateau, and $L_{\rm min}$ from the prompt emission, we obtain ϵ through Equation (10), which then fixes $\dot{m}_{\rm min}$, hence the propeller luminosity evolution and the propeller end time, i.e., the onset of the ejector phase. Two conclusions are apparent: (i) $L_{\rm prop}(t) \propto t^{-15/7}$ is well consistent with the steep decay observed at the end of the prompt phase and (ii) the onset of the plateau occurs at the time when $r_m \approx r_L$.

Similar results are obtained for all GRBs in our sample. For each of them, Table 3 shows the location of r_m at T_{min} and at the start of the plateau (T_{pl}): GRB 091029 and GRB 120404A match very well our model prediction, and the two short GRBs 130603B and 140903A are well consistent with it, given the time coverage of the available data. In the remaining five GRBs the plateau appears to start when r_m , though expanded by a large factor, is still $\sim (0.5-0.7)r_L$. In all of these five events, the prompt emission displays two or more peaks well separated in time, suggesting distinct accretion episodes with different start times relative to the GRB trigger. As shown, e.g., in Dall'Osso et al. (2017), such a temporal offset offers a simple interpretation for the apparent mismatch and may help reconcile these five GRBs with the basic picture proposed here. In particular, in order for $r_m \sim (0.9-1)r_L$ at the start of the plateau in these GRBs, an offset time $\sim (0.5-0.7)T_{\rm min}$ is typically required. A detailed modeling of this and other effects that may contribute to the light-curve shape is under way and will be presented in a forthcoming paper.

5. Summary and Conclusions

Several GRBs, characterized by a plateau in their X-ray afterglow light curves, have been modeled under the assumption of energy injection by a magnetar. In this work we have gone one step further in testing the presence of a magnetar central engine, by singling out a physical mechanism for accretion onto magnetic NSs—the transition to propeller—that has long been verified for NS in X-ray binaries and more recently validated for other classes of accreting stellar-mass objects (Campana et al. 2018). Under the assumption that the prompt emission of GRBs is powered by a phase of mass accretion toward a fast-spinning magnetar, we identified signatures of propeller transitions in the prompt light curves of GRBs. Based on such signatures, we estimated the minimum accretion luminosity, $L_{\rm min}$, in a sample of nine GRBs for which sufficient data are available.

We then estimated the dipolar magnetic field and the spin period of the NSs through fits to the X-ray afterglow plateaus. By combining these *independently* determined parameters according to Equation (2), we showed that the GRBs in our sample follow the same universal relation between L_{\min} , P, and B as other accreting, magnetic stellar-mass objects, albeit at a

¹⁶ Matter flung out by the propeller, if not unbound, may return to the disk and drift inward on viscous timescales (e.g., Li et al. 2021), by which time the ejector sweeps away the residual disk together with any recycled material, thus preventing significant effects on source luminosity.

¹⁷ We note in passing that our conclusion agrees with previous models showing that the millisecond magnetar spins down substantially only for propeller durations longer than hundreds of seconds (e.g., Piro & Ott 2011).

Table 3

Additional Physical Parameters of the Magnetar Central Engines Derived in Our GRB Sample

GRB	$\dot{m}_{ m min} \ (10^{-4} M_{\odot}/ m s)$	T _{min} (s)	$r_m(T_{\min})/R$	<i>T</i> _{pl} (s)	$r_L(T_{\rm pl})/R$	$r_m/r_L(T_{ m pl})$	$P(T_{\min})$ (ms)	$P(T_{\rm pl})$ (ms)	$\frac{\Delta M_{\rm acc}}{(10^{-3}M_{\odot})}$
060614	0.15	85	8.5	<4500	120.4	< 0.75	15.1	30.3	1.6
060729A	0.05	90	2.82	500	11.5	0.57	2.88	2.9	0.5
061222A	2.2	35	1.24	100	3.5	0.6	0.84	0.87	5.8
091029	1.0	10.5	1.83	130	6.1	0.99	1.50	1.54	1.3
100906A*	2.6	35	1.86	130	6.8	0.52	1.54	1.72	7.9
120404A*	5.6	6.5	2.3	110	10.1	0.9	2.13	2.54	4.6
130603B	1.7	0.09	7.7	< 30	52.9	<2.3	12.9	13.3	0.02
140903A	0.1	0.15	7.95	<100	54.5	< 3.2	13.6	13.7	0.005
151027A	1.3	60	2.01	350	7.95	0.6	1.73	2.00	8.1

Note. The mass accretion rate $\dot{m}_{\rm min}$ at $T_{\rm min}$ is calculated using ϵ from Table 2. The times $T_{\rm min}$ and $T_{\rm pl}$ are obtained directly from the prompt light curve. The magnetospheric radius r_m (in units of the NS radius, R) at $T_{\rm min}$ uses $\dot{m}_{\rm min}$ and the B-field derived from fits to the X-ray plateau. The light-cylinder radius r_L at the start time of the plateau ($T_{\rm pl}$) uses the best-fit spin period for the X-ray plateau, i.e., $P(T_{\rm pl})$. The value of $r_m(T_{\rm pl})$ is calculated from $r_m(T_{\rm min})$ using $\dot{m}_{\rm min}$ and the scaling $\dot{m} \propto t^{-5/3}$. $P(T_{\rm min})$ is the NS spin period at $T_{\rm min}$, calculated with our model for the propeller-induced spin-down. The last column features the total amount of mass that went through the disk during the propeller phase, i.e., between $T_{\rm min}$ and $T_{\rm pl}$.

lower radiative efficiency $\epsilon \sim 10^{-2} - 10^{-1}$. The latter is also in good agreement with independent observational constraints (e.g., Zhang et al. 2007) and theoretical expectations.

Moreover, by simply comparing the isotropic-equivalent luminosity of the X-ray plateau with that predicted by the NS spin-down model, we have estimated a conversion efficiency of spin-down power to afterglow emission $\sim 0.12-0.34$, remarkably consistent throughout our sample. This illustrates the diagnostic power of the ratio $L_{\min}/L_{p,X}$ (Equation (5)), which depends only on the NS spin period and the ratio of the radiative efficiencies $\epsilon/\epsilon_{\rm sd}$ in each source.

Our results demonstrate that a magnetar central engine can account at once for: (i) the prompt luminosity at the onset of the steep decay, the plateau duration and its luminosity in each individual GRB; (ii) a correlation among these properties in the GRB population, while simultaneously deriving radiative efficiencies of both accretion and spin-down in agreement with standard values; and (iii) the slope of the prompt steep decay, as well as the onset time of the plateau. The magnetar scenario we discussed—where accretion powers the GRB prompt emission and, once accretion subsides, the NS spin-down powers the afterglow plateau—is amenable to further development aimed at fitting the different stages of GRB light curves with a minimal set of model parameters. This will be the subject of future work.

We thank the anonymous referee for very helpful and insightful comments. This project has received funding from the European Unions Horizon 2020 Research and Innovation Programme under the Marie Skodowska-Curie (grant agreement No. 754496). R.P. kindly acknowledges support by NSF award AST-2006839. G.S. acknowledges the support by the State of Hesse within the Research Cluster ELEMENTS (Project ID 500/10.006). L.S. acknowledges financial contributions from ASI-INAF agreements 2017-14-H.O and I/037/12/0; from "iPeska" research grant (P.I. Andrea Possenti) funded under the INAF call PRIN-SKA/CTA (resolution 70/2016), and from PRIN-INAF 2019 No. 15. This work made use of data supplied by the UK Swift Science Data Centre at the University of Leicester.

ORCID iDs

Simone Dall'Osso https://orcid.org/0000-0003-4366-8265
Giulia Stratta https://orcid.org/0000-0003-1055-7980
Rosalba Perna https://orcid.org/0000-0002-3635-5677
Giovanni De Cesare https://orcid.org/0000-0003-0869-7180

Luigi Stella https://orcid.org/0000-0002-0018-1687

References

Abbott, B. P., Abbott, R., Abbott, T. D., et al. 2017, PhRvL, 119, 161101Aguilera-Miret, R., Viganò, D., Carrasco, F., Miñano, B., & Palenzuela, C. 2020, PhRvD, 102, 103006

Aguilera-Miret, R., Viganò, D., & Palenzuela, C. 2022, ApJL, 926, L31 Aksulu, M. D., Wijers, R. A. M. J., van Eerten, H. J., & van der Horst, A. J. 2022, MNRAS, 511, 2848

Aloy, M. Á, & Obergaulinger, M. 2021, MNRAS, 500, 4365 Andersson, N., Glampedakis, K., Haskell, B., & Watts, A. L. 2005, MNRAS, 361, 1153

Band, D., Matteson, J., Ford, L., et al. 1993, ApJ, 413, 281

Barthelmy, S. D., Baumgartner, W. H., Cummings, J. R., et al. 2009, GCN, 10103, 1

Barthelmy, S. D., Baumgartner, W. H., Cummings, J. R., et al. 2010, GCN, 11233, 1

Beniamini, P., Duque, R., Daigne, F., & Mochkovitch, R. 2020, MNRAS, 492, 2847

Beniamini, P., Giannios, D., & Metzger, B. D. 2017, MNRAS, 472, 3058 Beniamini, P., & Mochkovitch, R. 2017, A&A, 605, A60

Bernardini, M. G., Campana, S., Ghisellini, G., et al. 2013, ApJ, 775, 67

Bernardini, M. G., Campana, S., Ghisellini, G., et al. 2014, MNRAS, 439, L80 Bhattacharya, D., & van den Heuvel, E. P. J. 1991, PhR, 203, 1

Bucciantini, N., Metzger, B. D., Thompson, T. A., & Quataert, E. 2012, MNRAS, 419, 1537

Bucciantini, N., Quataert, E., Arons, J., Metzger, B. D., & Thompson, T. A. 2007, MNRAS, 380, 1541

Campana, S., Colpi, M., Mereghetti, S., Stella, L., & Tavani, M. 1998a,

Campana, S., Stella, L., Mereghetti, S., et al. 1998b, ApJL, 499, L65
Campana, S., Stella, L., Mereghetti, S., & de Martino, D. 2018, A&A,

610, A46 Cano, Z., Bersier, D., Guidorzi, C., et al. 2011, MNRAS, 413, 669 Chandra, P., & Frail, D. A. 2012, ApJ, 746, 156

Chirenti, C., Dichiara, S., Lien, A., Miller, M. C., & Preece, R. 2023, Natur, 613, 253

Ciolfi, R., Kastaun, W., Giacomazzo, B., et al. 2017, PhRvD, 95, 063016 Corbet, R. H. D. 1996, ApJL, 457, L31

Cromartie, H. T., Fonseca, E., Ransom, S. M., et al. 2020, NatAs, 4, 72 Dai, Z. G., & Lu, T. 1998, A&A, 333, L87

```
Dall'Osso, S., Giacomazzo, B., Perna, R., & Stella, L. 2015, ApJ, 798, 25
Dall'Osso, S., Perna, R., Tanaka, T. L., & Margutti, R. 2017, MNRAS,
   464, 4399
Dall'Osso, S., & Stella, L. 2022, in Astrophysics and Space Science Library,
   ed. S. Bhattacharyya, A. Papitto, & D. Bhattacharya, Vol. 465 (Cham:
Dall'Osso, S., Stella, L., & Palomba, C. 2018, MNRAS, 480, 1353
Dall'Osso, S., Stratta, G., Guetta, D., et al. 2011, A&A, 526, A121
D'Angelo, C. R., & Spruit, H. C. 2010, MNRAS, 406, 1208
Evans, P. A., Willingale, R., Osborne, J. P., et al. 2010, A&A, 519, A102
Filgas, R., Greiner, J., Schady, P., et al. 2012, A&A, 546, A101
Fong, W., Berger, E., Margutti, R., & Zauderer, B. A. 2015, ApJ, 815, 102
Frank, J., King, A., & Raine, D. J. 2002, Accretion Power in Astrophysics (3rd
   edn.; Cambridge: Cambridge Univ. Press)
Ghosh, P., & Lamb, F. K. 1979, ApJ, 234, 296
Giacomazzo, B., & Perna, R. 2013, ApJL, 771, L26
Giacomazzo, B., Zrake, J., Duffell, P. C., MacFadyen, A. I., & Perna, R. 2015,
    ApJ, 809, 39
Gibson, S. L., Wynn, G. A., Gompertz, B. P., & O'Brien, P. T. 2017, MNRAS,
   470, 4925
Gompertz, B. P., O'Brien, P. T., & Wynn, G. A. 2014, MNRAS, 438, 240
Guidorzi, C., Mundell, C. G., Harrison, R., et al. 2014, MNRAS, 438, 752
Guilet, J., Reboul-Salze, A., Raynaud, R., Bugli, M., & Gallet, B. 2022,
    MNRAS, 516, 4346
Heger, A., Fryer, C. L., Woosley, S. E., Langer, N., & Hartmann, D. H. 2003,
    ApJ, 591, 288
Hjorth, J., Sollerman, J., Møller, P., et al. 2003, Natur, 423, 847
Illarionov, A. F., & Sunyaev, R. A. 1975, A&A, 39, 185
Kawamura, T., Giacomazzo, B., Kastaun, W., et al. 2016, PhRvD, 94, 064012
Kiziltan, B., Kottas, A., De Yoreo, M., & Thorsett, S. E. 2013, ApJ, 778, 66
Kulkarni, A. K., & Romanova, M. M. 2013, MNRAS, 433, 3048
Kumar, P., Narayan, R., & Johnson, J. L. 2008, Sci, 321, 376
Kumar, P., & Zhang, B. 2015, PhR, 561, 1
Laskar, T., Berger, E., Margutti, R., et al. 2015, ApJ, 814, 1
Lattimer, J. M., & Prakash, M. 2001, ApJ, 550, 426
Li, S.-Z., Yu, Y.-W., Gao, H., & Zhang, B. 2021, ApJ, 907, 87
Lü, H.-J., & Zhang, B. 2014, ApJ, 785, 74
Lu, R.-J., Wei, J.-J., Qin, S.-F., & Liang, E.-W. 2012, ApJ, 745, 168
```

MacFadyen, A. I., & Woosley, S. E. 1999, ApJ, 524, 262

Margalit, B., & Metzger, B. D. 2017, ApJL, 850, L19

Mangano, V., Holland, S. T., Malesani, D., et al. 2007, A&A, 470, 105

Metzger, B. D., Thompson, T. A., & Quataert, E. 2007, ApJ, 659, 561

Nappo, F., Pescalli, A., Oganesyan, G., et al. 2017, A&A, 598, A23

Metzger, B. D., Beniamini, P., & Giannios, D. 2018, ApJ, 857, 95

```
Obergaulinger, M., & Aloy, M. Á 2021, MNRAS, 503, 4942
Oganesyan, G., Ascenzi, S., Branchesi, M., et al. 2020, ApJ, 893, 88
Palenzuela, C., Aguilera-Miret, R., Carrasco, F., et al. 2022, PhRvD, 106,
Palenzuela, C., Liebling, S. L., Neilsen, D., et al. 2015, PhRvD, 92, 044045
Palmer, D. M., Barthelmy, S. D., Cummings, J. R., et al. 2015, GCN, 18496, 1
Pan, Y. Y., Wang, N., & Zhang, C. M. 2013, Ap&SS, 346, 119
Parfrey, K., Spitkovsky, A., & Beloborodov, A. M. 2016, ApJ, 822, 33
Piro, A. L., Giacomazzo, B., & Perna, R. 2017, ApJL, 844, L19
Piro, A. L., & Ott, C. D. 2011, ApJ, 736, 108
Piro, L., Troja, E., Zhang, B., et al. 2019, MNRAS, 483, 1912
Pringle, J. E., & Rees, M. J. 1972, A&A, 21, 1
Racusin, J. L., Liang, E. W., Burrows, D. N., et al. 2009, ApJ, 698, 43
Radice, D. 2017, ApJL, 838, L2
Raynaud, R., Guilet, J., Janka, H.-T., & Gastine, T. 2020, SciA, 6, eaay2732
Rees, M. J. 1988, Natur, 333, 523
Rowlinson, A., O'Brien, P. T., Metzger, B. D., Tanvir, N. R., & Levan, A. J.
  2013, MNRAS, 430, 1061
Ryan, G., van Eerten, H., MacFadyen, A., & Zhang, B.-B. 2015, ApJ, 799, 3
Sakamoto, T., Sato, G., Barbier, L., et al. 2009, ApJ, 693, 922
Sari, R., Piran, T., & Halpern, J. P. 1999, ApJL, 519, L17
Siegel, D. M., Ciolfi, R., & Rezzolla, L. 2014, ApJL, 785, L6
Spitkovsky, A. 2006, ApJL, 648, L51
Stanek, K. Z., Matheson, T., Garnavich, P. M., et al. 2003, ApJL, 591, L17
Stella, L., Campana, S., Colpi, M., Mereghetti, S., & Tavani, M. 1994, ApJL,
  423, L47
Stella, L., White, N. E., & Rosner, R. 1986, ApJ, 308, 669
Stratta, G., Dainotti, M. G., Dall'Osso, S., Hernandez, X., & De Cesare, G.
  2018, ApJ, 869, 155
Tanvir, N. R., Levan, A. J., Fruchter, A. S., Hjorth, J., & Wiersema, K. 2013,
  GCN, 14893, 1
Thompson, C., & Duncan, R. C. 1995, MNRAS, 275, 255
Thompson, T. A., Chang, P., & Quataert, E. 2004, ApJ, 611, 380
Troja, E., Sakamoto, T., Cenko, S. B., et al. 2016, ApJ, 827, 102
Tsvetkova, A., Frederiks, D., Golenetskii, S., et al. 2017, ApJ, 850, 161
Tsvetkova, A., Frederiks, D., Svinkin, D., et al. 2021, ApJ, 908, 83
Ukwatta, T. N., Dhuga, K. S., Stamatikos, M., et al. 2012, MNRAS,
  419, 614
van Eerten, H. J. 2015, JHEAp, 7, 23
van Eerten, H., van der Horst, A., & MacFadyen, A. 2012, ApJ, 749, 44
Wang, X.-G., Zhang, B., Liang, E.-W., et al. 2018, ApJ, 859, 160
Zhang, B., Liang, E., Page, K. L., et al. 2007, ApJ, 655, 989
Zhang, B., & Mészáros, P. 2001, ApJL, 552, L35
Zrake, J., & MacFadyen, A. I. 2013, ApJL, 769, L29
```